Multiple structural components and their competition in the intermediate state of antiferroelectric $Pb(Zr,Ti)O_3$

Zheyi An,[1,*] Hiroko Yokota,[2,*] Nan Zhang,[1,†] Marek Paściak,[3,‡] Jan Fábry,[3] Miloš Kopecký,[3] Jiří Kub,[3] Guanjie Zhang,[1] A. M. Glazer,[4,§] T. R. Welberry,[5] Wei Ren,[1] and Zuo-Guang Ye[6]

[1]*Electronic Materials Research Laboratory, Key Laboratory of the Ministry of Education & International Center for Dielectric Research, School of Electronic Science and Engineering, Xi'an Jiaotong University, Xi'an 710049, China*

[2]*Department of Physics, Chiba University, 1-33 Yayoi-cho, Inage-ku, Chiba City 263-8522, Japan and JST PRESTO, 7 Goban-cho, Chiyoda-Ku, Tokyo 102-0076, Japan*

[3]*Institute of Physics of the Czech Academy of Sciences, Na Slovance 2, 182 21 Prague 8, Czech Republic*

[4]*Department of Physics, University of Oxford, Parks Road, Oxford OX1 3PU, United Kingdom and Department of Physics, University of Warwick, Gibbet Hill Road, Coventry CV4 7AL, United Kingdom*

[5]*Research School of Chemistry, Australian National University, Canberra ACT 2601, Australia*

[6]*Department of Chemistry and 4D LABS, Simon Fraser University, 8888 University Drive, Burnaby, British Columbia, Canada V5A 1S6*

(Received 29 October 2020; revised 17 January 2021; accepted 3 February 2021; published 23 February 2021)

Antiferroelectric perovskites form an important family of functional electric materials, which have high potential in energy storage and conversion applications. However, a full understanding of their crystal structural formation is still lacking. $PbZrO_3$-based materials can serve as a model system for investigation, not only because $PbZrO_3$ was the first discovered antiferroelectric, but also because it undergoes a typical phase transition sequence from a high-temperature paraelectric to the low-temperature antiferroelectric phase, passing through a possible intermediate phase that is poorly understood. Here we employ a combination of optical and scattering experiments and theoretical calculations to reveal the nature of the intermediate state. Evidence is found that this peculiar state consists of multiple short-range and long-range structural components, and their competition is crucial in stabilizing the antiferroelectric phase. External stimuli such as temperature change or chemical substitution can easily alter each component's energy landscape and thereby change the materials' electrical properties. These findings provide insights into understanding antiferroelectric-ferroelectric competition and can be useful in designing alternative antiferroelectric materials.

DOI: 10.1103/PhysRevB.103.054113

I. INTRODUCTION

Antiferroelectrics (AFEs) are characterized by antiparallel cation displacements in their crystal structure and electric-field induced AFE to ferroelectric (FE) phase transitions [1]. As the most widely used AFE material, $PbZrO_3$ (PZ) has received much attention in fundamental studies and applications such as actuators and energy storage devices [2]. However, there are still many unanswered questions about PZ and PZ-related solid solutions [such as $PbZr_{1-x}Ti_xO_3$ (PZT), with $x \leqslant 0.06$]. Understanding the existence and nature of the intermediate (IM) structure [3–5] between the room-temperature AFE *Pbam* [6] and high-temperature paraelectric (PE) $Pm\bar{3}m$ phases is crucial in this sense.

The IM phase in PZ was first observed in ceramics by Shirane *et al.* [7] and in single crystals by Scott and Burns [5], marked by dielectric permittivity and remnant polarization anomalies. Interestingly, the temperature range of this phase varies in different samples, and sometimes it only occurs on cooling but not on heating [7]. This was also frequently observed in several types of doped-PZ systems, and the choice of dopants is considered to affect the appearance and stabilization of the IM phase [8]. Its observation is sometimes related to the high-temperature superstructure reflection intensities, such as at M points $\{h/2\ k/2\ l\}_{pc}$ (subscript pc denotes the pseudocubic coordinate system throughout this paper), and at incommensurate points, observed via electron diffraction [9–11], and x-ray [12,13] and neutron scattering experiments [14,15], but not all these types of superstructure intensities appear in each case. High-resolution transmission electron microscopy (TEM) studies [16–18] reported different modulated high-temperature structures in doped PZ ceramics. Their possible formations were also suggested by lattice dynamics studies [19–21], which show that on cooling through the transition temperature T_C, phonon softening happens at various intermediate positions of the type $(\xi, \xi, 0)$, in addition to the Brillouin zone center and zone boundary. Theoretical calculations predict unstable phonon branches and energetically competing phases featuring structural modulations with wave vectors along the same direction [22–24]. Besides Pb modulations, high-temperature short-range ordered (SRO) oxygen octahedral tilts [4,11,25–27] are also observed and

*These authors contribute equally to this work.
†nzhang1@xjtu.edu.cn
‡pasciak@fzu.cz
§mike.glazer@physics.ox.ac.uk

considered to be important in the stabilization of the AFE phase [19,20,23].

Despite all these characterizations, the proposed structural models to describe the IM phase are still somewhat controversial. Furthermore, the phase-change process is not clear, especially on how the IM structure leads to the stabilized AFE phase. The distinct existence of the IM phase provides an opportunity to observe and analyze the stabilization process of the AFE phase. However, the IM phases usually exist only in a narrow temperature interval in PZ [4], and therefore it is hard to capture them. On the other hand, with a small amount of Ti substitution, the temperature range of the IM phase becomes wider [28,29]. At the same time, the main structural features appearing in pure PZ are maintained, which makes a detailed study of the IM structures possible.

In this work, we have investigated the IM phase of $PbZr_{1-x}Ti_xO_3$ ($x \leqslant 0.06$) single crystals and ceramics to reveal its local and average structures and the process of structural transformation with temperature. Optical experiments, neutron, and x-ray scattering results show that the IM phase is not a pure phase but a state containing a mixture of several short- and long-range correlated structural components that compete with each other energetically in a complicated way. To emphasize this, we shall henceforth refer to it as the IM *state* rather than the IM *phase*.

II. EXPERIMENTAL DETAILS

A. Crystal growth

Zr-rich PZT single crystals were grown using the flux-growth method. Pb_3O_4, ZrO_2, and TiO_2 were weighed according to the stoichiometric composition of $PbZr_{0.93}Ti_{0.07}O_3$ to form the solution. The Ti concentrations in the as-grown crystals, on the other hand, are less than 7%, and with possible composition segregations in large areas of the crystals. The exact compositions were determined using optical experiments and will be described in detail in the Results section. The type and amount of flux (Pb_3O_4, B_2O_3) and the temperature profile were the same as in the previous lead zirconate crystal growth procedure [26]. The growth was carried out in an uncovered Pt crucible and placed in a cylindrical furnace, the axial temperature gradient of which was lower than $1.5\,^{\circ}\mathrm{C\,cm^{-1}}$. The as-grown crystals were washed by immersing the solidified flux in 30% HNO_3 solution. Two selected crystals, namely, crystals 1 and 2, were polished parallel to the $\{001\}_{pc}$ planes with a thickness of ~0.08 mm for optical measurements and diffraction experiments. The dimensions were around $1.2 \times 1.15\,\mathrm{mm^2}$ for crystal 1 and $0.65 \times 0.32\,\mathrm{mm^2}$ for crystal 2.

B. Birefringence imaging microscopy (BIM) and composition determination

The optical measurements were performed using BIM equipment (Metripol, Oxford Cryosystems Ltd.). Monochromatic light with a wavelength of 590 nm served as the light source. The light passes through the crystal sample after transmitting through a Polaroid (P_1), rotating about the microscope axis at a frequency of ω. The light is then focused by an objective lens before passing through a quarter-wave plate and a Polaroid (P_2). Finally, the intensity measured by a charge-coupled device (CCD) camera as a function of ω is given by

$$I = \tfrac{1}{2} I_0 \{1 + \sin[2(\omega t - \varphi)] \sin\delta\},$$

where I_0 is the intensity of the incident light, t is the time, φ is the angle between the horizontal direction and the principal axis of the optical indicatrix of the sample, and δ is the phase shift introduced to the light due to the anisotropy of the sample. During the measurements, the intensity I at each pixel position was measured for ten equal polarizer P_1 angles, so that $|\sin\delta|$ and φ values are obtained [30]. For the high-temperature experiments, the crystals were heated from room temperature up to 250 °C at a rate of $2\,^{\circ}\mathrm{C\,min^{-1}}$ with a Linkam (THMS600E) heating stage.

C. Diffuse scattering experiment and data processing details

Diffuse scattering experiments were carried out at Beamline X-Ray Diffraction I at the Elettra Sincrotrone Trieste, Italy. The x-ray energy was set to be 13 keV (0.9537 Å), just below the "L_3" absorption edge of Pb 13.035 keV [31]. Scattering data were accumulated by rotation of the crystals around the ω axis with $\Delta\omega = 0.25^{\circ}$ steps. The exposure time was 5 s per frame. The intensity was collected by a PILATUS 2M pixel area detector (Dectris, Switzerland). The distance between the detector and the crystal was 105 mm for crystal 1 and 85 mm for crystal 2. The measurements were carried out at a series of temperatures above 100 °C and below 250 °C with an interval of 5°C–10 °C. The data were processed with the SNBL Toolbox [32], while reciprocal-space planes were reconstructed with the program CRYSALIS and self-developed MATLAB scripts.

D. Ceramic preparation and x-ray total scattering measurement

Ceramic samples having nominal compositions $PbZr_{0.95}Ti_{0.05}O_3$ and $PbZr_{0.94}Ti_{0.06}O_3$ were used in this study, and the preparation conditions are described in Yokota *et al.* [33]. In order to verify the Ti concentration in the sintered ceramic samples, Rietveld refinements against neutron diffraction data collected in the cubic phase were performed. For $PbZr_{0.95}Ti_{0.05}O_3$, refinement of the data at 240 °C shows Ti occupancy is 0.055(3); for $PbZr_{0.94}Ti_{0.06}O_3$, the refined Ti occupancy at 250 °C is 0.064(3) (see the Supplemental Material [34] for details of refinements). For simplicity, these samples are referred to by their nominal compositions throughout this paper. X-ray total scattering experiments were carried out at the I15-1 beamline at the Diamond Light Source, UK, using synchrotron x rays (wavelength $\lambda = 0.161669$ Å, 76.69 keV). A small amount of powdered ceramic was loaded into a borosilicate glass capillary of 1 mm (outer) diameter. A hot-air blower was used to heat the capillary samples. The data were collected from room temperature to 300 °C. Two detectors were placed at different distances and positions to obtain two datasets with a large Q range (up to $38.86\,\mathrm{Å^{-1}}$) and decent reciprocal-space resolution. Dataset 1 was used to refine the lattice parameters and sample densities. Dataset 2 was first corrected for background, multiple scattering, Compton scattering, and absorption, and then Fourier transformed into

pair distribution function (PDF) patterns, using the program GUDRUNX [35]. Small-box modeling of the PDF data was performed using the software PDFFIT [36].

E. High-resolution neutron diffraction

Neutron time-of-flight experiments were performed at HRPD, ISIS (Rutherford Appleton Laboratory, UK). Data collected from the backscattering detector bank were selected for structural refinement, with the highest resolution $\Delta d/d \approx 6 \times 10^{-4}$. Data were collected at 200 °C in the 10–110 ms time of flight windows covering the 0.21–2.28 Å d-spacing range.

Rietveld refinement was carried out using TOPAS ACADEMIC [37]. The scale factor, background parameters, peak-shape function parameters, and absorption correction coefficient were refined.

F. *Ab initio* calculations

Theoretical structural calculations were carried out within the DFT GGA (Wu-Cohen) approximation [38] as implemented in the SIESTA program package [39]. Semicore states were included as valence in the norm-conserving Troullier-Martins pseudopotentials. The conjugate-gradient method was used for all optimizations, with the convergence criteria being 0.01 eV Å^{-1} for forces and 0.1 GPa for stresses. An equivalent $8 \times 8 \times 8$ k-grid mesh per simple perovskite unit cell was used with a mesh cutoff of 400 Ry. The FINDSYM program [40] was used for the evaluation of the symmetry of the optimized structures.

III. RESULTS

A. Identification of the IM state

X-ray diffuse scattering (DS) experiments were first performed to identify the phase transition process for crystal 1 and crystal 2 upon heating. They were carried out on a selected small region on each crystal, and the region sizes depended on the x-ray beam sizes, being $100 \times 100\,\mu m^2$ for crystal 1, and $120 \times 80\,\mu m^2$ for crystal 2. Considering the fact that the measured regions are small, they can be regarded as of homogeneous composition. To determine the exact compositions of these two regions, they were then marked and carefully studied under BIM. In the entire regions of the crystals, the Curie temperatures observed under BIM range from 232 °C to 244 °C for crystal 1 and from 232 °C to 241 °C for crystal 2 upon heating. In the regions selected for DS experiments on crystal 1, the IM state happens between 195 °C (T_{IM}) and 239 °C (T_C), corresponding to a Ti concentration around 3% [41]; for the selected region on crystal 2, T_{IM} is 190 °C, and T_C is 234 °C, with Ti concentration being around 1% [41].

The crystals have an antiferroelectric *Pbam* structure [6] below T_{IM}, marked by strong $\{h/4\ k/4\ l\}_{pc}$ (quarter) reflections in the diffraction patterns [Fig. 1(a)] and 45 °/0 ° optical domains projected on the $\{001\}_{pc}$ plane [Fig. 1(d)]. In the AFE phase, M-point reflections exist but are very weak [Fig. 1(a)]. Furthermore, there are sharp DS lines passing through some quarter reflections along $\langle 110\rangle_{pc}$, caused by antiphase boundaries (APBs) separating two domains with

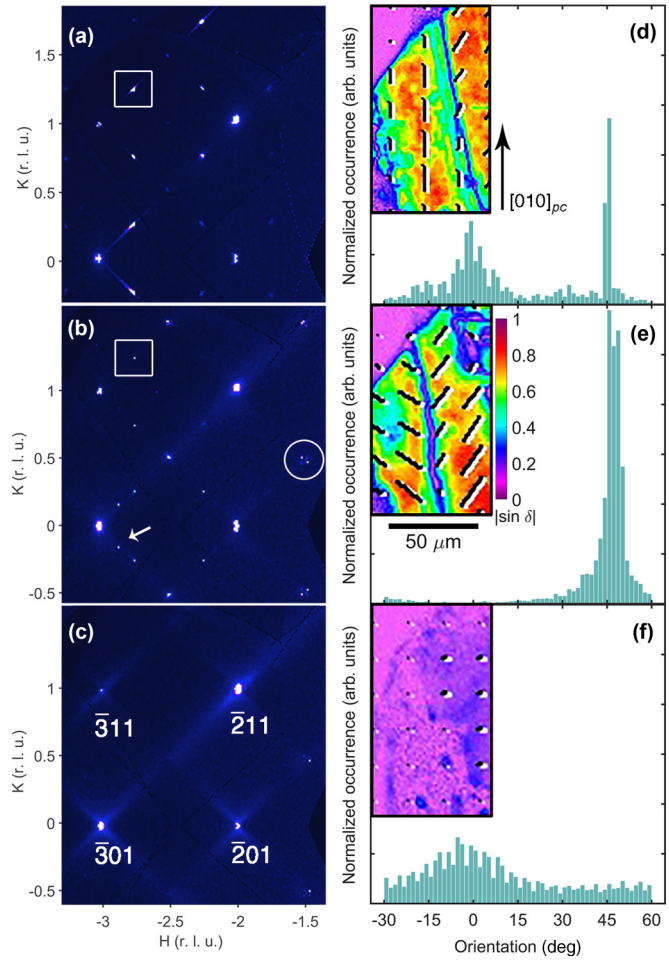

FIG. 1. Reciprocal space maps and domain configurations of a PZT single crystal (crystal 1) in AFE, IM, and cubic phases. (a)–(c) X-ray scattering data on the (h k 1) plane at 150 °C (AFE phase), 215 °C (IM state), and 240 °C (cubic phase), respectively. The square and circle indicate a typical quarter and M-point reflection, respectively. The arrow points to the incommensurate spot. Insets of (d)–(f) show mappings of $|\sin\delta|$ values from the same area of the crystal at 140 °C (AFE phase), 232 °C (IM state), and 240 °C (cubic phase), respectively. Black lines are projections of the principal optic axes on the $\{001\}_{pc}$ plane, indicating ferroelastic domain orientations. Histograms of the orientations are shown in (d)–(f).

phase-shifted antiparallel cation displacements, which have also been reported at a similar composition [42]. In the BIM image [Fig. 1(d) inset], orthorhombic domains with polarizations along $[110]_{pc}$ and $[011]_{pc}$ coexist [43]. Figure 1(d) shows the distribution histogram of the orientations obtained over all pixels in the displayed BIM image. Two peaks centered at 0 ° and 45 ° are observed. It should be noted that the 0 ° peak is broader than the 45 ° peak, which indicates that the polarizations are likely to be distributed in the $\langle 11x\rangle_{pc}$ directions ($x \neq 0$) and are different across the whole bulk. In other words, there may exist short-range correlated out-of-plane polarizations, similar to that speculated by Teslic and Egami [15].

Under BIM, the IM state is observed at T_{IM} when a large number of domains appear, leading to a rapid increase of

domain walls and decreased birefringence. The ending of the IM state and the arrival of the cubic phase are marked by the disappearance of domain walls and zero birefringence (see the movie in the Supplemental Material [34] for a demonstration of the transition process). Both AFE-IM and IM-PE phase transitions are of first order, as there is thermal hysteresis observed for T_C (1 °C) and for T_{IM} (12 °C). In the IM state, no domains with 0 ° orientation exist, as shown in Fig. 1(e). Traditionally, the IM structure was determined in the space group $R3m$ [3,44], in which the polarization is oriented at 45 °. However, in our observation, the orientations of domains are distributed around a value slightly larger than 45 °, which indicates that the IM structure may not be of rhombohedral symmetry. The diffraction pattern changes significantly on entering the IM state [Fig. 1(b)]. Quarter reflections and APB DS lines become weaker, indicating the diminishing of the antiferroelectric *Pbam* structure. Between some Bragg and quarter reflections in the $\langle 110\rangle_{pc}$ directions, intensities at incommensurate (IC) points start to appear. The IC reflections are given by $\{h \pm 0.16\ k \pm 0.16\ l\}_{pc}$ (calculated from the reflection positions plotted in Fig. S1(a) of the Supplemental Material [34]). This indicates that the IC modulation is between 6 and 7 unit cells, consistent with most of the IC structures observed in doped PZ ceramics by electron microscopy [17].

Meanwhile, in the IM state, the M points become distinctly visible and start to split, with satellite peaks appearing. Intensities are found at the M points, both when $h = k$ and $h \neq k$, and are considerably strengthened in the IM state. As the oxygen octahedral tilts only give rise to $h \neq k$ M or R points [45], at least a certain amount of the M-point intensities in our crystals must be due to alternating single $\langle 110\rangle_{pc}$ rows of distinct cation displacements (mainly Pb^{2+}) in directions or lengths. Here, we denote this general structural feature as the *M-type structure*. The antiparallel cation displacement model was also proposed in PZ and PZT ($x \leqslant 0.06$) ceramics in previous studies [9,10,15]. The peculiar satellites of the M points are another feature throughout the entire IM state. The three-dimensional distribution of DS intensities around each M point (Fig. S1(b) of the Supplemental Material [34]) demonstrates that the satellites are along the $\langle 111\rangle_{pc}$ directions. This indicates a further modulation along $\langle 111\rangle_{pc}$, possibly separated by APBs [13,46]. The vectors from the center of the M point to those of the satellites were determined as $\langle 0.02\ 0.02\ 0.02\rangle_{pc}$ in reciprocal lattice units. This corresponds to modulations with widths of 50 unit cells in real-space, similar to the estimate by Andronikova *et al.* [13].

B. Phase-change process

Detailed diffraction patterns and DS intensities at various temperatures during the phase-change process on heating of two pieces of crystals are shown in Fig. 2. At 150 °C [Fig. 2(a)], quarter reflections are strong, and M-point intensities are weak. Figure 2(b) shows the beginning of the transition at which the IC emerges. This demonstrates the interruption of the long-range ordered *Pbam* structure and the beginning of disordering. Upon further heating, strengthening and splitting of the M points occur [Fig. 2(c)]. Simultaneously, the IC and quarter reflections weaken and finally disappear on approaching T_C [Fig. 2(d)]. The M-point intensities also tend to weaken at this temperature. Figure 2(e) depicts the change of superstructure reflection intensities over smaller temperature intervals. IC points start appearing at 180 °C, while M-point intensities start strengthening and splitting at 200 °C. Quarter reflections do not disappear entirely until 225 °C, indicating that the M-type, AFE, and IC superstructures coexist in a broad temperature range. Figures 2(f)–2(j) show a slightly different scenario in crystal 2. Under the same experimental conditions as crystal 1, IC points appear at a higher temperature than the strengthening of the M-point intensities, opposite to the process in crystal 1. The IC structure exists in an interval of 20 °C just below T_C, and the strong M-point intensities with satellites cover the whole IM state.

Combining the diffraction and DS intensity changes of these two crystals, one may conclude that in bulk material, different volumes with individual local superstructural features are in competition. The integrated intensities (Fig. 3) show that the increase of some reflections is at the expense of others. The intensity exchange among the quarter, M, and IC points indicates an active exchange of phase-component volumes over the entire IM state. The formation of IC regions may be at lower or higher temperatures compared to the M-type structure, but the AFE and the incommensurate modulated regions tend to transform into the M-type structure eventually. This makes the strengthening of M-point intensities and their satellites the most significant features of the IM state and shows that before the crystals change into the cubic phase, this M-type structure is the most stable among all three types of superstructures.

In the context of the much-discussed role of the tilted oxygen octahedra in the AFE phase transition mechanism, it is also important to pay some attention to the tilt signatures in the scattering signal that we observe. Previous works [26,27,47] show that rather significant SRO of tilts exists in the cubic phase of both PZ and Zr-rich PZT. This SRO manifests itself in the form of diffuse scattering lines connecting $M\ \{h/2\ k/2\ l\}_{pc}$ and $R\ \{h/2\ k/2\ l/2\}_{pc}$ points in reciprocal space. Images of a half-plane section containing both M and R points at several temperatures are shown in Fig. 4. A weak but clear DS line is found in the cubic phase [Fig. 4(c) and 4(d)] and disappears altogether in the IM state [Figs. 4(a) and 4(b)]. This means that the high-temperature SRO tilted octahedra become ordered over substantially larger scales, and the scattered intensity must have transferred to either M (plus tilts) or R points (minus tilts) [45]. It is observed in Fig. 3 that the intensity gains at the R point are visible only at lower temperatures, which strongly resemble those of the quarter reflections and thus can be safely associated with the AFE structure and its $a^-a^-c^0$ tilts (Glazer's notation, meaning that the oxygen octahedral tilt by the same angle about $[100]_{pc}$ and $[010]_{pc}$, with successive octahedra along each direction tilted in antiphase, while there is no tilt about $[001]_{pc}$ [45]). Therefore, one may deduce that in the IM state, most of the tilts turn into longer-range in-phase tilts and contribute to the increased intensities of M points along with antiparallel Pb^{2+} displacements. These in-phase tilts may play an important role in stabilizing some of the IM structures, and appear as a natural intermediate step between the cubic phase with SRO

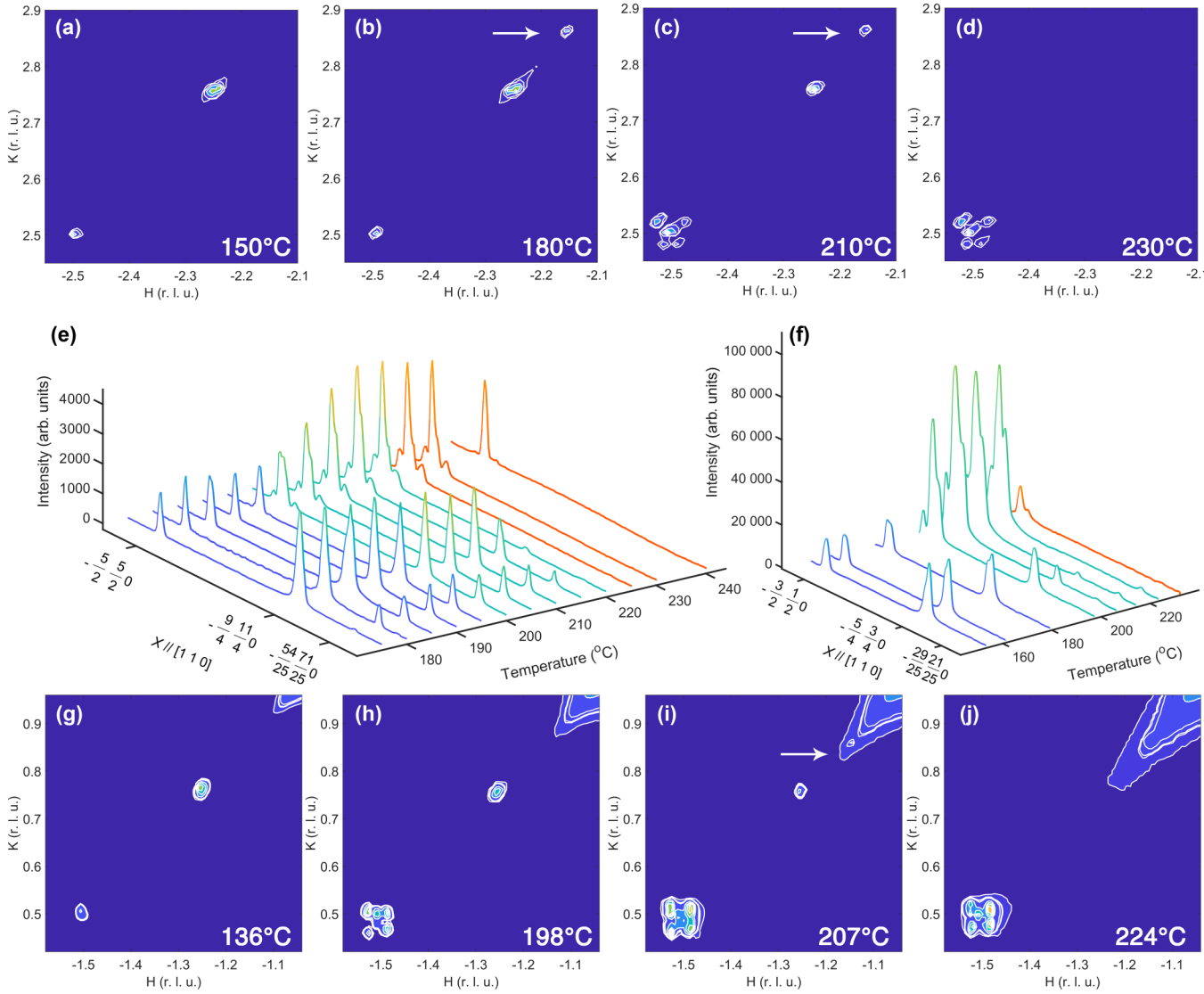

FIG. 2. Diffraction patterns and DS intensities during phase-change process of two crystals. (a)–(d) Data containing M point (–2.5 2.5 0), quarter reflection (–2.25 2.75 0), and IC spot (–2.16 2.84 0) collected from crystal 1 at 150 °C, 180 °C, 210 °C, and 230 °C, respectively. (g)–(j) Data containing M point (–1.5 0.5 0), quarter reflection (–1.25 0.75 0), and IC spot (–1.16 0.84 0) collected from crystal 2 at 136 °C, 198 °C, 207 °C, and 224 °C, respectively. The arrows point to the IC points. It should be noted that due to the structure factor being additive for $h + k + l =$ even, diffuse scattering around (–1 1 0) is stronger than that around (–2 3 0). Three-dimensional (3D) intensity was integrated over a range in l corresponding to around ± 0.1 reciprocal lattice unit (r.l.u.) to produce two-dimensional (2D) patterns. (e), (f) Intensity developments along $[110]_{pc}$ at more temperatures. One-dimensonal (1D) diffraction pattern was obtained by integrating 2D images over a range along $[-1\ 1\ 0]_{pc}$ with ± 0.1 r.l.u. width.

tilts and the long-range $a^-a^-c^0$ tilts of the AFE structure. The latter configuration with strong rotation-related correlations propagating in all directions might be more easily disrupted by Ti^{4+} ions, which would explain why the M-type structure is commonly observed even for minimal Ti content but not in pure PZ.

C. Refinements of IM structures

To obtain systematic information about the short- and long-range M-type structural models in the IM state, we carried out powder x-ray total scattering and high-resolution neutron diffraction experiments on PZT powder samples with high-Zr concentrations. The diffraction data show that they possess virtually the same phase-change procedure as in our single-crystal samples, marked by a similar development of M-point intensities and quarter reflections (Fig. S2 of the Supplemental Material [34]). As shown in Fig. 5(a), M-point intensities are observed and are maintained almost unchanged from 210 °C to 240 °C, indicating that the IM structure is stabilized with little remnant AFE structure in this temperature range.

Small-box modeling was first performed against the PDF data of PZT ($x = 0.05$) collected at 210 °C with r-range between 3 and 12.9 Å. Models with different lattices, sizes of configuration, and symmetry restrictions were tried. The best fit [Fig. 5(b)] was obtained using a model with the coexistence of two phases (denoted as Phase 1 and Phase 2), each being a 2 × 2 × 1 pseudocubic unit cell. The lattice parameters were set

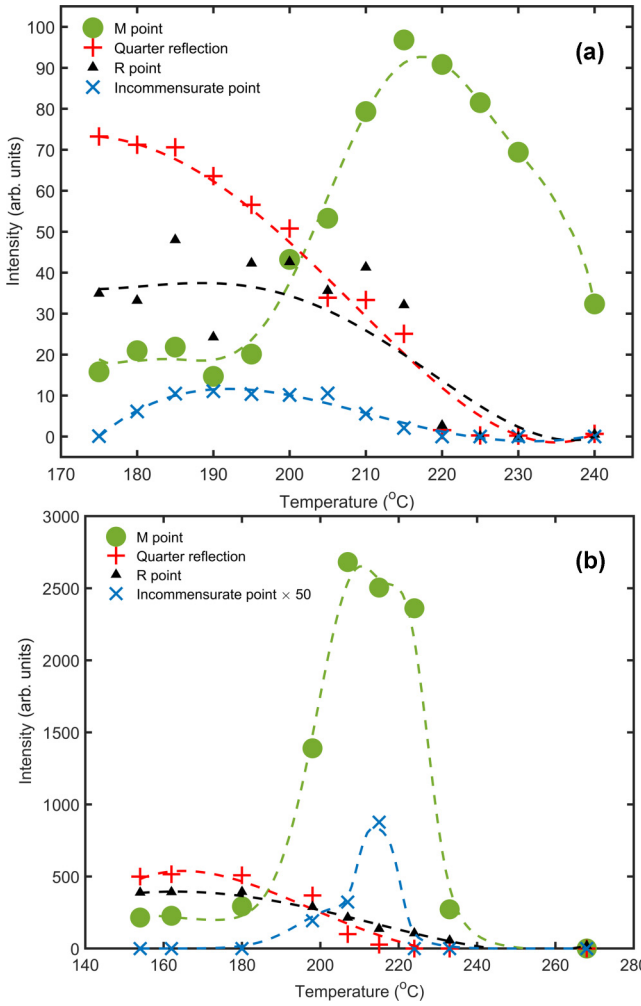

FIG. 3. Integrated DS intensities of superstructure reflections evolving with temperature. 1D intensities of reflections in the same area on the main planes, as in Figs. 2(d) and 2(e), and on half plane (h k 0.5), were integrated along $[110]_{pc}$. (a) M point (−2.5 2.5 0), quarter reflection (averaged over −2.25 2.75 0 and −1.75 3.25 0), IC point (averaged over −2.16 2.84 0 and −1.84 3.16 0), and R point (−1.5 2.5 0.5) on crystal 1. (b) M point (−1.5 0.5 0), quarter reflection (−1.25 0.75 0), and R point (−1.5 −1.5 0.5) on crystal 2. The intensity of the weak IC point (−1.16 0.84 0) in (b) was multiplied by 50 to make it visible. The dashed lines are a guide for the eyes.

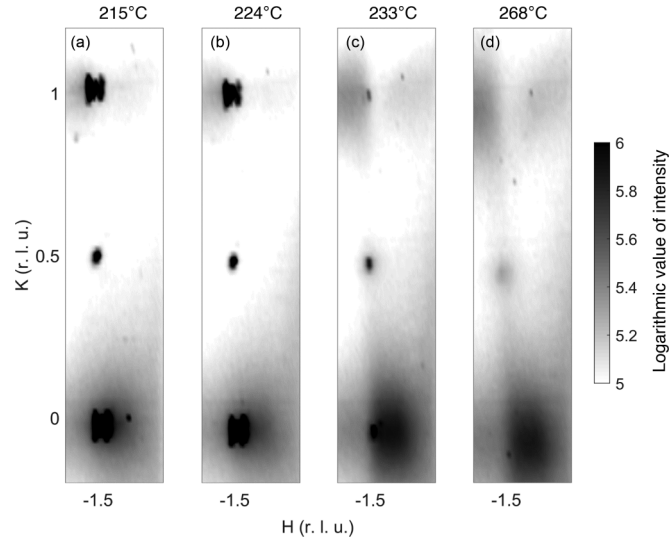

FIG. 4. The diffuse scattering intensity with crystal 2 of a selected region on the (h k 0.5) plane evolving with temperature. 3D intensity was integrated over a range in l corresponding to ± 0.1 r.l.u. to produce 2D patterns.

as $a = b \neq c$, $\alpha = \beta = 90°$, $\gamma \neq 90°$, and the cations were allowed to be displaced along the $[11x]_{pc}$ direction. The refined IM structural parameters of these two coexisting phases are shown in Table I. The calculated and experimental PDF patterns, and the PDFs calculated from each phase are shown in Fig. 5(b). As we have noticed, both in the refined lattice parameters and fitted pattern, the two phases have different lattice parameters and volumes, with the unit cell in Phase 1 larger than that in Phase 2. The slightly different bond lengths originating from this unit-cell size difference enable an almost perfect fitting of the strongly asymmetrical peaks around 3.6, 7, and 9.1Å. With only one phase, it is impossible to satisfy these peak intensities, thus further establishing the validity of such a phase coexistence at the local scale.

In addition to the lattice parameters, the in-plane $[(001)_{pc}$ plane] displacements of Pb^{2+} are also aligned differently in these two phases. The structural models of Phase 1 and Phase 2 are shown in Figs. 5(d) and 5(e), respectively. In both phases, we assigned the in-plane displacements of four Pb^{2+} to be independent of each other during fitting. The

TABLE I. Short-range structural parameters obtained from x-ray PDF refinement (3–12.9 Å) of $PbZr_{0.95}Ti_{0.05}O_3$ ceramic powder.

X-ray PDF refinement of $PbZr_{0.95}Ti_{0.05}O_3$ at 210 °C, reduced χ^2: 6.34%							
Phase 1 Unit-cell volume (Å^3): 293.0(8)				Phase 2 Unit-cell volume (Å^3): 283.7(6)			
a (Å)	c (Å)	γ (deg)	scale (%)	a (Å)	c (Å)	γ (deg)	scale (%)
8.291(9)	4.262(8)	89.5(5)	50(2)	8.257(7)	4.162(6)	89.0(2)	50(2)
Atoms	x	y	z	Atoms	x	y	z
Pb1	0.235(5)	0.235(5)	0.6(1)	Pb5	0.247(5)	0.247(5)	0.60(1)
Pb2	0.272(5)	0.772(5)	0.6(2)	Pb6	0.236(6)	0.736(6)	0.56(3)
Pb3	0.772(5)	0.272(5)	0.6(2)	Pb7	0.736(5)	0.236(5)	0.56(3)
Pb4	0.735(5)	0.735(5)	0.6(1)	Pb8	0.735(4)	0.735(4)	0.54(2)

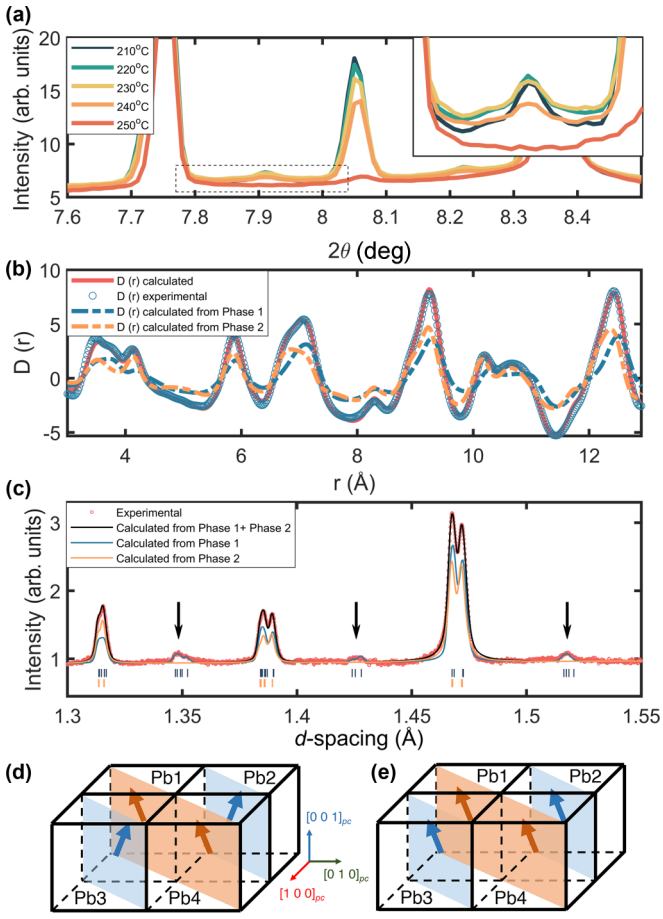

FIG. 5. Powder diffraction and modeled local structure in the IM state. (a) X-ray total scattering intensity ($\lambda = 0.161\,669$ Å) in the 2θ range between $\{222\}_{pc}$ and $\{321\}_{pc}$ with $PbZr_{0.95}Ti_{0.05}O_3$ ceramic powder at 210 °C−250 °C. Inset of (a) zoomed-in plot of an *M*-point reflection, the position of which corresponds to $\{7/2\ 1/2\ 0\}_{pc}$, $\{5/2\ 5/2\ 0\}_{pc}$, and $\{3/2\ 5/2\ 2\}_{pc}$. (b) Experimental PDF pattern generated from total scattering data at 210 °C and the best-fit PDF. Dashed lines indicate the fitted PDF components of Phase 1 and Phase 2. (c) Experimental (red) and refined (black) HRPD data with $PbZr_{0.94}Ti_{0.06}O_3$ ceramic powder at 200 °C with arrows indicating *M*-point positions. Blue and orange lines indicate the calculated patterns from Rietveld-refined Phase 1 (*Pc*) and Phase 2 (*Cm*) structures, respectively. Logarithmic values of intensities are used to demonstrate the low-intensity *M* points. Full-range data are shown in Fig. S4 of the Supplemental Material [34]. (d), (e) Schematic drawings of modeled Phase 1 and 2 structures, respectively. The arrows represent displacement vectors of Pb cations. The orange arrows (Pb1 and Pb4) and planes belong to chain I while the blue ones (Pb2 and Pb3) belong to chain II.

result shows that, in Phase 1, two alternating chains along $\langle 110\rangle_{pc}$ are spontaneously formed, and the Pb^{2+} cations in the neighboring chains always have opposite in-plane displacement directions [Fig. 5(d)]. On the other hand, in Phase 2, all four Pb^{2+} cations possess the same in-plane displacement directions, even if they are in different chains [Fig. 5(e)]. As shown in Table I, the scale factors for these two phases are close, indicating that their proportions in the bulk material should be similar at 210 °C. From small-box modeling at higher temperatures up to 240 °C, the percentage of Phase 1 stays around 50% below T_C, consistent with the single-crystal DS results in which the *M*-point intensities remain almost unchanged after the *M*-type structure is stabilized [Figs. 2(e) and 2(f)].

Long-range structural models with the same in-plane arrangements as the PDF fitted Phase 1 (space group *Pc*) and Phase 2 (space group *Cm*) were constructed and Rietveld refined [48] with high-resolution neutron powder diffraction HRPD data at 200 °C for $PbZr_{0.94}Ti_{0.06}O_3$. Note that from total scattering data (Fig. S3 of the Supplemental Material [34]), both the local and average structures of $PbZr_{0.95}Ti_{0.05}O_3$ and $PbZr_{0.94}Ti_{0.06}O_3$ in the IM state are similar. The fitted structural models and the conversion relationship from the monoclinic to pseudocubic unit cells are shown in Table II. The result of the fitting is shown in Fig. 5(c) and Fig. S4 of the Supplemental Material [34], in which the Bragg and the *M*-point intensities were successfully reproduced. In Phase 1, both the in-plane antiparallel Pb^{2+} displacements and oxygen tilts introduced by the *c*-glide plane (along the $y_{\text{monoclinic}}$ direction) were refined. The refinement results show that the O2/O3 fractional displacements resulting from in-phase tilts are 0.007(2), smaller than the antiparallel Pb^{2+} displacement value 0.0136(9). This suggests that significant contribution to the *M*-point intensities is the Pb^{2+} displacements, with some in-phase tilts present. In our refinement, Pb^{2+} displacements along $z_{\text{monoclinic}}$ are almost zero, indicating that the Pb^{2+} cations are indeed antiparallel on the $\{110\}_{pc}$ plane in the average structure. Some high-resolution TEM results on other PZ-based doped systems [16] show that in specific local regions, Pb^{2+} cations deviate from the $\{110\}_{pc}$ plane with nonzero $z_{\text{monoclinic}}$ displacements, which is also allowed in space group *Pc*. The refined scale ratio of *Pc* and *Cm* phases is around 1:1, similar to the PDF analysis results. Since it is difficult to observe other superstructure reflections from powder diffraction data (such as IC points), we deduce that the real structure in the IM state consists of the long-range correlated Phase 1 and Phase 2 with about the same proportion, and several short-range correlated superstructure components.

In the PDF and Rietveld refinement results, the out-of-plane components (along z_{pc}) of the displacements are rather large. This indicates that both the length and correlation of the out-of-plane displacements increase from zero when the structure changes from AFE to IM during heating. This is similar to that suggested by Teslic and Egami [15]. At the same time, the correlated out-of-plane displacements give rise to a net polarization, which determines the ferroelectric nature of the IM state, even though in Phase 1 the in-plane displacements are antiparallel. Also, the fact that the cation displacements have different in-plane and out-of-plane projections further confirms the existence of monoclinic instead of rhombohedral symmetry in the IM state.

In our average structural refinement, both phases are close to being metrically rhombohedral as the a_{pc}, b_{pc}, and c_{pc} values are closely similar (Table II). However, the polarization directions are not along $\langle 111\rangle_{pc}$ but may rotate on (or near) the $\{110\}_{pc}$ plane. With multiple local components, similar lattice parameters conveniently allow domains to coexist at multiple length scales. In the IM state, the optical orientation from the BIM experiments is only slightly away from 45° on the $\{001\}_{pc}$ plane. This reflects the pseudorhombohedral

TABLE II. Long-range structural parameters from Rietveld refinement of high-resolution neutron diffraction data with $PbZr_{0.94}Ti_{0.06}O_3$ ceramic powder at 200 °C. The atom positions are in the monoclinic settings.

Rietveld refinement of $PbZr_{0.94}Ti_{0.06}O_3$ at 200 °C, r_{wp}: 2.83%, r_p: 2.89%							
Phase 1 (*Pc*) scale: 48(1)% r_{Bragg}: 0.84%				Phase 2 (*Cm*) scale: 52(1)% r_{Bragg}: 0.75%			
Lattice vectors: $\vec{a}_m = \vec{c}_{pc}, \vec{b}_m = \vec{a}_{pc} - \vec{b}_{pc}, \vec{c}_m = \vec{a}_{pc} + \vec{b}_{pc}$				Lattice vectors: $\vec{a}_m = \vec{a}_{pc} + \vec{b}_{pc}, \vec{b}_m = \vec{b}_{pc} - \vec{a}_{pc}, \vec{c}_m = \vec{c}_{pc}$			
a_m (Å)	b_m (Å)	c_m (Å)	β(deg)	a_m (Å)	b_m (Å)	c_m (Å)	β(deg)
4.15578(6)	5.8631(1)	5.8817(1)	89.779(1)	5.8811(1)	5.8627(2)	4.1521(2)	89.788(2)
$a_{pc}(b_{pc})$ (Å)	c_{pc} (Å)	$\alpha(\beta)$ (deg)	γ (deg)	$a_{pc}(b_{pc})$ (Å)	c_{pc} (Å)	$\alpha(\beta)$ (deg)	γ (deg)
4.15240(6)	4.15578(6)	89.8433(8)	89.818(2)	4.15208(6)	4.1521(2)	89.850(1)	89.821(2)
Atoms	x	y	z	Atoms	x	y	z
Pb	0.014(7)	0.7636(9)	0.005(7)	Pb	−0.002(1)	0	0.064(4)
Zr(Ti)	0.513(8)	0.2509(6)	0.005(4)	Zr(Ti)	0.483(2)	0	0.564(3)
O1	0.029(8)	0.25	0.027(4)	O1	0.4240(7)	0	−0.018(2)
O2	0.477(6)	0.507(2)	0.243(2)	O2	0.228(3)	0.246(2)	0.547(9)
O3	0.5	0.007(2)	0.257(2)				

nature of the crystal, and the determinations of an intermediate rhombohedral symmetry in the past probably relied on measurements of the lattice parameters [3] rather than on the crystal structure. However, our short- and long-range structural refinements show no threefold symmetry axis as far as atom displacements are concerned. The existence of low-symmetry monoclinic phases potentially leads to high piezoelectric properties at high temperatures for the compositions near pure PZ, similar to what is known in the morphotropic phase boundary (MPB) region [49,50].

TABLE III. Structural parameters from quantum mechanical structural optimizations for $PbZrO_3$.

*Pma*2			
Lattice vectors: $\vec{a}_o = \vec{a}_{pc} - \vec{b}_{pc}, \vec{b}_o = \vec{a}_{pc} + \vec{b}_{pc}, \vec{c}_o = \vec{c}_{pc}$			
	a_o (Å)	b_o (Å)	c_o (Å)
	5.87399	5.91678	4.20514
Atoms	x	y	z
Pb	0.25	0.7943	0.0877
Zr	0.25	0.2628	0.5281
O1	0.25	0.2157	0.0032
O2	0	0	0.4665
O3	0	0.5	0.4672
Pc			
Lattice vectors: $\vec{a}_m = \vec{c}_{pc}, \vec{b}_m = \vec{a}_{pc} - \vec{b}_{pc}, \vec{c}_m = \vec{a}_{pc} + \vec{b}_{pc}$			
a_m (Å)	b_m (Å)	c_m (Å)	β (deg)
4.20904	5.86585	5.86120	89.521
Atoms	x	y	z
Pb	0.0668	0.7824	0.0411
Zr	0.5238	0.2598	0.0073
O1	0.0052	0.2376	−0.0224
O2	0.4875	0.5484	0.1999
O3	0.4690	0.0257	0.2692

D. DFT calculations

To gain further support for the proposed structures of IM Phases 1 and 2, we have performed quantum mechanical structural optimizations for pure PZ using density functional theory (DFT). As the first step, the Pb-shift configuration characteristic for the IM Phase 1 [Fig. 5(d)] was relaxed with the conjugate-gradient method, effectively treating only the atoms that were moved from their cubic symmetry positions. This has resulted in a *Pma*2 structure (Table III) with energy 99 meV/formula unit (meV/fu) above the *Pbam* ground state compared with 305 meV/fu in the cubic state. All atoms were then set to relax freely, ending with an atomic configuration of *Pc* symmetry (Table III) with distinct in-phase octahedral tilts and energy 61 meV/fu. This energy is lower than any of the nontilted phases (lowest in our calculation—in agreement with Íñiguez *et al.* [23]—is the *R*3*m* phase with 77 meV/fu). Multiple trials with small random oxygen atom shifts as initial conditions did not reveal any lower-energy tilt pattern compatible with the preoptimized Pb^{2+} displacements. We also went on to optimize the IM Phase 2, starting from the *Pc* structure modified by aligning all Pb^{2+} displacements [as in Fig. 5(e)]. With fixed-strain relaxation, the Pb^{2+} shifts remain roughly aligned in a structure with small residual forces (0.02 eV $Å^{-1}$) and energy only 3 meV/fu above *Pc*, but then the optimization process drives it back to the *Pc* structure. Its stability may depend on external factors such as Ti^{4+} substitution or other dopants.

IV. CONCLUSIONS

The IM state contains several local-structural components, including IM Phase 1, IM Phase 2, an AFE residue, and incommensurate structures. As exemplified above, these components are expected to be very close in energy. Their proportions in a specific composition can be roughly estimated by

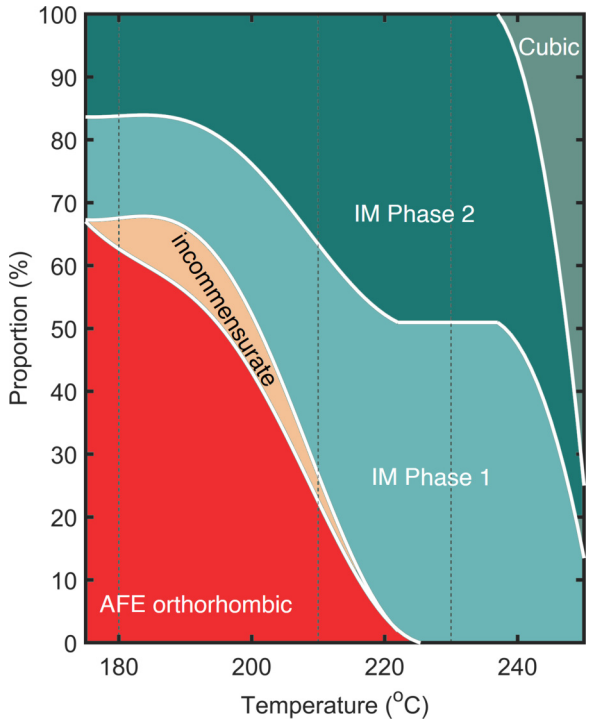

FIG. 6. Competition among local-structural components. Schematic diagram showing the proportions of local-structural components as a function of temperature in a typical AFE PZT crystal. Proportions of components at a certain temperature equal to the intersection of this diagram and a vertical line at this temperature. The dashed lines correspond to the cases discussed in Figs. 2(b)–(d), respectively.

calculating the ratios among AFE, IC, and IM Phase 1 based on the quarter, IC, and *M*-point x-ray scattering intensities. The relative proportions of IM Phase 1 and IM Phase 2 for compositions near $x = 0.06$ is around 1:1. This ratio may vary by further changing with the Ti concentration, depending on the energy change of these two phases. The competition between IM Phase 1 and IM Phase 2 may heavily influence whether it is the AFE ($x \leqslant 0.06$) or FE ($x > 0.06$) structure that is stabilized at room temperature. A schematic plot of the proportions of local-structural components as a function of temperature is shown in Fig. 6. It should be noted that this diagram corresponds mainly to the volume change of *local-structural* components, and so for a large temperature range below T_{IM}, several IM phases already appear in the form of possible local disorders. This makes the "phase boundary" between the AFE phase and the IM state indistinct at the local scale and different from the established PZT phase diagrams [28,41,44]. The estimated proportion in the figure is approximate because only one arbitrary superstructure reflection of each type was considered, and the difference in the structure factors of different $\{h\ k\ l\}$ was not taken into account. However, for one type of reflection, the change of its intensity with temperature is positively correlated to the volume change of its representing structure. The schematic plot is suitable for one particular AFE composition. With a small composition change, virtually the same structural components should appear in the IM state, but their relative proportions and transition temperatures will be somewhat different.

There is a particular mixture of structural components that can transform into one another at any specific temperature. Before the IM state is stabilized, we observe a period of intense domain wall movements optically (see Supplemental Movie [34]). This may be the result of volume exchange among all the structural components. Small external stimuli or chemical modifications can induce the change of the metastable states for one or more components. This may explain the discrepancy in the observed behavior of the IM state among different samples, especially with different types of dopants or substitutions [8].

In this study, we have demonstrated the existence and competition of several superstructure components in the intermediate state connecting the low-temperature AFE and high-temperature cubic structures. This provides experimental evidence for multiple-point phonon softening, which had been theoretically predicted [22–24] and is related to the room-temperature stabilization of the AFE mode. The monoclinic IM Phase 1 and Phase 2 are particularly important, as they may serve as the basis for several possible variants before turning into AFE or FE phases on cooling. Their subtle balance may be related to the critical Ti substitution (∼6%), that is right on the border between the room-temperature AFE and FE phases and is also the location of a high-temperature tricritical point [41]. Our work demonstrates the highly complex nature of the crystal structures occurring near this composition.

ACKNOWLEDGMENTS

N.Z., Z.A., and G.Z. are supported by the NSFC (Grants No. 12074304 and No. 51911530121) and the "111 Project" of China (B14040). M.P. is supported by the Strategy AV21 framework of the Czech Academy of Sciences, Efficient Energy Conversion and Storage program. For the synchrotron experiment at Elettra, support was received under the CALIPSOplus project under Grant Agreement No. 730872 from the EU's HORIZON 2020 research and innovation framework program. H.Y. is supported by the Ministry of Education, Culture, Sports, Science and Technology in Japan for financial support (Grant No. 17K05489) and JST PRESTO Grant No. JPMJPR19LA, Japan. Z.-G.Y. acknowledges support from the U.S. Office of Naval Research (ONR, Grant No. N00014-16-1-3106) and the Natural Sciences and Engineering Research Council of Canada (NSERC, Grant No. RGPIN-2017-06915). We are also grateful to Elettra Sincrontrone Trieste for access to Beamline X-Ray Diffraction I (Experimental Session No. 20195557), the Diamond Light Source for Beamline I15-1 (Experimental Sessions No. EE17368 and No. EE19968), and the ISIS neutron spallation source for the HRPD instrument. The computational part of this research was undertaken at the NCI National Facility in Canberra, Australia, supported by the Australian Commonwealth Government.

[1] C. Kittel, Phys. Rev. **82**, 729 (1951).
[2] A. S. Mischenko, Q. Zhang, J. F. Scott, R. W. Whatmore, and N. D. Mathur, Science **311**, 1270 (2006).
[3] G. Shirane and S. Hoshino, Phys. Rev. **86**, 248 (1952).
[4] J.-H. Ko, M. Górny, A. Majchrowski, K. Roleder, and A. Bussmann-Holder, Phys. Rev. B **87**, 184110 (2013).
[5] B. A. Scott and G. Burns, J. Am. Ceram. Soc. **55**, 331 (1972).
[6] D. L. Corker, A. M. Glazer, J. Dec, K. Roleder, and R. W. Whatmore, Acta Crystallogr., Sect. B **53**, 135 (1997).
[7] G. Shirane, E. Sawaguchi, and Y. Takagi, Phys. Rev. **84**, 476 (1951).
[8] R. Faye, H. Liu, J.-M. Kiat, B. Dkhil, and P.-E. Janolin, Appl. Phys. Lett. **105**, 162909 (2014).
[9] J. Ricote, D. L. Corker, R. W. Whatmore, S. A. Impey, A. M. Glazer, J. Dec, and K. Roleder, J. Phys.: Condens. Matter **10**, 1767 (1998).
[10] D. I. Woodward, J. Knudsen, and I. M. Reaney, Phys. Rev. B **72**, 104110 (2005).
[11] D. Viehland, Phys. Rev. B **52**, 778 (1995).
[12] R. G. Burkovsky, I. A. Bronwald, D. A. Andronikova, B. Wehinger, M. Krisch, J. Jacobs, D. Gambetti, K. Roleder, A. Majchrowski, A. V. Filimonov *et al.*, Sci. Rep. **7**, 41512 (2017).
[13] D. A. Andronikova, I. A. Bronwald, N. G. Leontyev, I. N. Leontyev, D. Y. Chernyshov, A. V. Filimonov, and S. Vakhrushev, Phys. Solid State **61**, 1772 (2019).
[14] H. Fujishita, J. Phys. Soc. Jpn. **61**, 3606 (1992).
[15] S. Teslic and T. Egami, Acta Crystallogr., Sect. B **54**, 750 (1998).
[16] T. Ma, Z. Fan, B. Xu, T. H. Kim, P. Lu, L. Bellaiche, M. J. Kramer, X. Tan, and L. Zhou, Phys. Rev. Lett. **123**, 217602 (2019).
[17] H. He and X. Tan, Phys. Rev. B **72**, 024102 (2005).
[18] Z. Fu, X. Chen, Z. Li, T. Hu, L. Zhang, P. Lu, S. Zhang, G. Wang, X. Dong, and F. Xu, Nat. Commun. **11**, 3809 (2020).
[19] A. K. Tagantsev, K. Vaideeswaran, S. Vakhrushev, A. V. Filimonov, R. G. Burkovsky, A. Shaganov, D. A. Andronikova, A. I. Rudskoy, A. Q. R. Baron, H. Uchiyama *et al.*, Nat. Commun. **4**, 2229 (2013).
[20] J. Hlinka, T. Ostapchuk, E. Buixaderas, C. Kadlec, P. Kužel, I. Gregora, J. Kroupa, M. Savinov, A. Klic, J. Drahokoupil *et al.*, Phys. Rev. Lett. **112**, 197601 (2014).
[21] R. G. Burkovsky, A. K. Tagantsev, K. Vaideeswaran, N. Setter, S. B. Vakhrushev, A. V. Filimonov, A. Shaganov, D. Andronikova, A. I. Rudskoy, A. Q. R. Baron, H. Uchiyama, D. Chernyshov, Z. Ujma, K. Roleder, A. Majchrowski, and J.-H. Ko, Phys. Rev. B **90**, 144301 (2014).
[22] P. Ghosez, E. Cockayne, U. V. Waghmare, and K. M. Rabe, Phys. Rev. B **60**, 836 (1999).
[23] J. Íñiguez, M. Stengel, S. Prosandeev, and L. Bellaiche, Phys. Rev. B **90**, 220103(R) (2014).
[24] B. Xu, O. Hellman, and L. Bellaiche, Phys. Rev. B **100**, 020102(R) (2019).
[25] N. Zhang, H. Yokota, A. M. Glazer, and P. A. Thomas, Acta Crystallogr., Sect. B **67**, 461 (2011).
[26] N. Zhang, M. Paściak, A. M. Glazer, J. Hlinka, M. Gutmann, H. A. Sparkes, T. R. Welberry, A. Majchrowski, K. Roleder, Y. Xie *et al.*, J. Appl. Crystallogr. **48**, 1637 (2015).
[27] M. Paściak, T. R. Welberry, A. P. Heerdegen, V. Laguta, T. Ostapchuk, S. Leoni, and J. Hlinka, Phase Transitions **88**, 273 (2015).
[28] F. Cordero, F. Trequattrini, F. Craciun, and C. Galassi, Phys. Rev. B **87**, 094108 (2013).
[29] E. Buixaderas, T. Ostapchuk, J. Kroupa, M. Savinov, I. Gregora, and J. Hlinka, Phase Transitions **87**, 1105 (2014).
[30] A. M. Glazer, J. G. Lewis, and W. Kaminsky, Proc. R. Soc. London, Ser. A **452**, 2751 (1996).
[31] J. H. Hubbell and S. M. Seltzer, Tables of x-ray mass attenuation coefficients and mass energy-absorption coefficients 1 keV to 20 MeV for elements $Z = 1$ to 92 and 48 additional substances of dosimetric interest, National Institute of Standards and Technology Report No. NISTIR-5632, 1995.
[32] V. Dyadkin, P. Pattison, V. Dmitriev, and D. Y. Chernyshov, J. Synchrotron Radiat. **23**, 825 (2016).
[33] H. Yokota, N. Zhang, A. E. Taylor, P. A. Thomas, and A. M. Glazer, Phys. Rev. B **80**, 104109 (2009).
[34] See Supplemental Material at http://link.aps.org/supplemental/10.1103/PhysRevB.103.054113 for more details on data analysis and structural refinements, and a movie showing the phase transition of a crystal under BIM.
[35] A. K. Soper and E. R. Barney, J. Appl. Crystallogr. **44**, 714 (2011).
[36] C. L. Farrow, P. Juhas, J. W. Liu, D. Bryndin, E. S. Boin, J. Bloch, T. Proffen, and S. J. L. Billinge, J. Phys.: Condens. Matter **19**, 335219 (2007).
[37] A. A. Coelho, J. Appl. Crystallogr. **38**, 455 (2005).
[38] Z. Wu and R. E. Cohen, Phys. Rev. B **73**, 235116 (2006).
[39] J. M. Soler, E. Artacho, J. D. Gale, A. García, J. Junquera, P. Ordejón, and D. Sánchez-Portal, J. Phys.: Condens. Matter **14**, 2745 (2002).
[40] H. T. Stokes and D. M. Hatch, J. Appl. Crystallogr. **38**, 237 (2005).
[41] R. W. Whatmore, R. Clarke, and A. M. Glazer, J. Phys. C: Solid State Phys. **11**, 3089 (1978).
[42] S. Vakhrushev, D. A. Andronikova, D. Y. Chernyshov, A. V. Filimonov, S. A. Udovenko, and N. V. R. Kumar, *X-Ray Scattering by Antiphase Ferroelectric Domain Walls in the Antiferroelectric Phase of the* $PbZr_{0.985}Ti_{0.015}O_3$ edited by O. Galinina, S. Andreev, S. Balandin, and Y. Koucheryavy (Springer, Cham, 2018).
[43] A. A. Bokov, X. Long, and Z.-G. Ye, Phys. Rev. B **81**, 172103 (2010).
[44] B. Jaffe, W. R. Cook, and H. Jaffe, *Piezoelectric Ceramics* (Academic Press, London, 1971).
[45] A. M. Glazer, Acta Crystallogr., Sect. B **28**, 3384 (1972).
[46] Z. Fu, X. Chen, P. Lu, C. Zhu, H. Nie, F. Xu, G. Wang, and X. Dong, Cryst. Growth Des. **18**, 4395 (2018).
[47] D. A. Andronikova, I. A. Bronwald, I. N. Leontiev, N. G. Leontiev, D. Y. Chernyshov, A. V. Filimonov, and S. Vakhrushev, Ferroelectrics **538**, 65 (2019).
[48] H. Rietveld, J. Appl. Crystallogr. **2**, 65 (1969).
[49] N. Zhang, H. Yokota, A. M. Glazer, Z. Ren, D. A. Keen, D. S. Keeble, P. A. Thomas, and Z.-G. Ye, Nat. Commun. **5**, 5231 (2014).
[50] N. Zhang, H. Yokota, A. M. Glazer, D. A. Keen, S. Gorfman, P. A. Thomas, W. Ren, and Z.-G. Ye, IUCrJ **5**, 73 (2018).